Journal of Catalysis 280 (2011) 125–136

Contents lists available at ScienceDirect

Journal of Catalysis

journal homepage: www.elsevier.com/locate/jcat

Characterization of alumina-supported Pt and Pt–Pd NO oxidation catalysts with advanced electron microscopy

O.K. Ezekoye [a], A.R. Drews [b], H.-W. Jen [b], R.J. Kudla [b], R.W. McCabe [b], M. Sharma [b], J.Y. Howe [c], L.F. Allard [c], G.W. Graham [a,*], X.Q. Pan [a]

[a] Department of Materials Science and Engineering, University of Michigan, Ann Arbor, MI 48109-2136, United States
[b] Chemical Engineering Department, Research and Innovation Center, Ford Motor Company, Dearborn, MI 48121-2053, United States
[c] Materials Science & Technology Division, Oak Ridge National Laboratory, Oak Ridge, TN 38731, United States

ARTICLE INFO

Article history:
Received 12 October 2010
Revised 14 March 2011
Accepted 16 March 2011
Available online 19 April 2011

Keywords:
NO oxidation catalysts
Pt
Pt–Pd alloys
Aberration-corrected TEM

ABSTRACT

Alumina-supported Pt and Pt–Pd catalysts for NO oxidation were fabricated from two different precursors, acetylacetonate and nitrate. A variety of electron microscopy techniques, notably aberration-corrected scanning transmission electron microscopy, were used to investigate both sets of catalysts in the fresh state (air calcined at 300 °C, then reduced in 1% H_2 at 300 or 500 °C) and after oxygen-rich hydrothermal aging at 500 °C and 900 °C. Aberration-corrected microscopy and spectroscopic analysis revealed a significant difference in particle size and composition between the two fresh bimetallic catalysts, with the catalyst made from nitrate precursors containing relatively large (3–10 nm) Pd-rich particles in addition to smaller (1–2 nm) Pt-rich particles that were typical of the acetylacetonate precursors. Regardless of initial state, however, bimetallic particles underwent similar degrees of growth and homogenization (alloying) with aging. In particular, particle growth in the bimetallic catalysts from both precursors was limited relative to that in the pure Pt catalysts, where anomalously large (~500 nm) particles formed at 900 °C, and the bimetallic catalysts from both precursors thus showed similar improvements in thermal stability, with little effect on measured NO reaction rates.

1. Introduction

Lean-burn gasoline and diesel engines increase fuel economy over conventional gasoline engines for transportation applications, but the catalytic after-treatment of exhaust, notably NO_x and soot, presents unique additional challenges. Accordingly, after-treatment technology has been extended beyond the familiar three-way catalyst to include NO_x storage and release catalysts, selective catalytic reduction catalysts, and diesel particulate filters. Improved durability and lower precious metal loading remain important goals for further development, however.

NO oxidation is a critical step in both of the NO_x reduction processes and soot oxidation, and Pt remains the preferred NO oxidation catalyst. Previous studies have shown that excessive Pt particle coarsening, an important deactivation mechanism for supported Pt catalysts, occurs readily under lean conditions [1]. Although the mechanisms are not understood, alloying Pt with other metals is known to inhibit such particle growth. Several years ago, for example, Chen and Schmidt found that alloying Pt with Pd suppressed particle growth (and/or volatile loss of Pt) on a planar SiO_2 support that was heated in air [2]. More recently, some of us demonstrated that substitution of Pd for up to 50 at.% of the Pt in alumina-supported catalysts reduced particle growth during lean aging with little or no impact on the NO oxidation turn-over frequency [3]. Although these catalysts were made using Pt- and Pd-acetylacetonate precursors in an attempt to promote alloying in the earliest phases of particle formation [4,5], we were not able to directly confirm that individual metal particles in the fresh or even slightly aged bimetallic catalysts contained both metals.

The present work thus focuses on an extension of our previous study of alumina-supported Pt and Pt–Pd catalysts, making use of advanced electron microscopy techniques that allow investigation of both particle size and composition in the fresh state as well as the changes induced by lean aging. In particular, we report results obtained using emerging electron microscopy techniques such as aberration-corrected scanning transmission electron microscopy (STEM) in high-angle annular dark-field (HA-ADF) imaging mode, along with more established techniques such as energy dispersive spectroscopy (EDS) and conventional TEM imaging.

In addition, we contrast these results from catalysts made with acetylacetonate precursors with those obtained from a new set of Pt and Pt–Pd catalysts prepared from nitrate precursors and produced via incipient wetness, a widely used, commercially

* Corresponding author. Fax: +1 734 763 4788.
E-mail address: gwgraham@umich.edu (G.W. Graham).

0021-9517/$ - see front matter © 2011 Elsevier Inc. All rights reserved.
doi:10.1016/j.jcat.2011.03.011

advantageous method for large scale production of heterogeneous catalysts [6].

2. Experimental details

2.1. Catalyst preparation and aging

Two catalyst compositions, both having a nominal precious metal loading equivalent (in molar terms) to approximately 1 wt.% Pt, were used for this study: the first contained only Pt (labeled Pt100–Pd0), and the second was a 50 mol% combination of Pt and Pd (labeled Pt50–Pd50). Catalysts of both compositions were synthesized using two different methods. The first set, (labeled AcAc) was prepared previously [3] by adsorption from mixtures of solutions of platinum(II) and palladium(II) bis-acetylacetonates in toluene at 70 °C onto a high-surface-area alumina (W.R. Grace, MI-307). After drying at 70 °C under vacuum, these catalysts were calcined at 300 °C in 5% O_2 in N_2 and reduced in 1% H_2 in N_2 at 300 °C.

The second set of catalysts (labeled Nitrate) was prepared by impregnating the same high-surface-area alumina with mixtures of aqueous Pt- and Pd-nitrate solutions to incipient wetness. After impregnation, the support/solution mixtures were homogenized, dried, and calcined at 300 °C in air for 1 h. The actual metal loadings for both sets of catalysts used in this study are summarized in Table 1.

Aliquots of each fresh catalyst were aged in a quartz-tube furnace under a flowing (5 l/min) gas mixture of 5% O_2 and 10% H_2O in N_2 at both 500 °C and 900 °C for 3 h (heating and cooling occurred under pure N_2). Before examination, all samples were reduced for 1 h at 500 °C under flowing 1% H_2 in N_2.

2.2. Microscopy characterization

Particle size, morphology, and composition were characterized using TEM. Samples were prepared for TEM examination by ultrasonicating a small amount of powder in ethanol and dispersing it on a 300 mesh carbon-coated copper grid. Because of the reported difficulty in direct imaging of small (diameter <2 nm) metal particles using conventional electron microscopy [3], an aberration-corrected STEM/TEM instrument was used to obtain structural information for catalysts in the fresh state. This instrument, a JEOL 2200FS fitted with a hexapole aberration corrector (CEOS GmbH) for the probe-forming optics, is capable of sub-100 pm spatial resolution in STEM mode. Further details of this instrument, located in the Advanced Microscopy Laboratory (AML) at Oak Ridge National Laboratory (where it is available through the High Temperature Materials Laboratory's National User program), can be found in earlier reports [7,8].

HA-ADF imaging was also performed on a Hitachi HF-3300, operated at 300 kV with STEM resolution 0.2 nm. The HF-3300, which is also located at the AML, was equipped with an integrated Thermo-Noran EDX analyzer for compositional analysis. The Cliff–Lorimer integration method (without absorption) was used to quantify the compositional results [9].

Table 1
Catalyst designations and compositions.

Catalyst name	Composition (wt.%)		Atom fraction		Equivalent Pt (wt.%)
	(Pt)	(Pd)	(Pt)	(Pd)	
Pt100–Pd0 AcAc	0.87	0	100	0	0.87
Pt50–Pd50 AcAc	0.58	0.28	53	47	1.09
Pt100–Pd0 Nitrate	0.87	0	100	0	0.87
Pt50–Pd50 Nitrate	0.58	0.28	53	47	1.09

Quantitative particle size analysis for aged catalysts was performed with a JEOL 3011, with a point-to-point resolution of 0.17 nm, which is located in the Electron Microbeam Analysis Laboratory (EMAL) at The University of Michigan.

Histograms characterizing the size distribution of three-dimensional (3-D) particles (as distinguished from single atoms and rafts in Sections 3.1.1 and 3.2.1) were created for each catalyst sample from TEM observation of approximately 100 particles. A surface-weighted mean diameter, d_s, was subsequently obtained from these distributions using Eq. (1), where n refers to the number of particles with diameter d.

$$d_s = \frac{\sum nd^3}{\sum nd^2} \tag{1}$$

Previously reported electron microscopy results and Monte-Carlo simulations indicate that such particles typically have a cubo-octohedral shape. Assuming a spherical or cubo-octohedral particle shape, dispersion, D, can be calculated from the surface-weighted mean diameter using the following expression:

$$D = 6\frac{M}{N_A \rho a d_s} \tag{2}$$

where d_s, surface-weighted mean diameter; M, atomic mass; N_A, Avogadro's number; ρ, mass density of the particle; a, area occupied by an atom on the particle surface.

Following the procedure of Morfin and others, equal proportions of the (1 1 1), (1 0 0), and (1 1 0) planes on the particle surface were assumed [4], and thus the surface area occupied by an atom on the particle surface is 0.0807 nm^2 for Pt [5] and 0.079 nm^2 for Pd [10]. For bimetallic catalysts, this parameter was derived from the atomic proportions of the constituent metal atoms.

2.3. X-ray diffraction characterization

X-ray diffraction (XRD) data from the Nitrate catalysts were collected in a Scintag X2 diffractometer equipped with a Si(Li) solid state detector using Cu Kα radiation and configured in Bragg–Bretano focusing geometry. Diffraction data were obtained over the range 10–90° (2θ) in steps of 0.03°. XRD samples were prepared by packing powder into a shallow cavity etched into a glass plate. Peaks in the background-subtracted scan were profile-fit using a Pearson 7 function [11] to characterize the breadth and position of the precious-metal peaks. Crystallite sizes were estimated from the corrected XRD peak breadths using a Scherrer analysis of the (3 1 1) peak of the fcc lattice (located near 81.2° for Pt), assuming spherical particles.

Because both platinum and palladium crystallize in a face-centered cubic (fcc) lattice and are isostructural, the effects of alloying on the XRD peaks are manifested only by changes in the observed lattice parameter and the relative peak intensities. For the aged catalyst samples, the lattice parameter for the fcc phase was estimated from the positions of the (1 1 1), (2 0 0) and (3 1 1) peaks. In the case of the Pt50–Pd50 catalyst, poor peak intensities only allowed fitting of the (3 1 1) peak.

2.4. Catalytic testing

NO oxidation measurements were performed on the Nitrate catalysts using a 10-channel flow reactor manufactured by Altamira Instruments that has been described previously [12a]. Experimental conditions were matched to those previously described for the AcAc catalysts [3]. Briefly, reactor tubes were loaded with 50 mg of catalyst sample and fixed between quartz wool plugs. Steady-state measurements were performed at a series of temperatures from 75 to 325 °C, following a standard 90 min equilibration at each temperature (shown in all cases to produce stable reactor

outlet concentrations). The feed gas composition was a mixture of 500 ppm NO and 8% O_2 in N_2 at a flow rate of 60 sccm in each channel (space velocity = 20,000 h^{-1}).

For selected catalysts and aging conditions, NO conversion vs. temperature profiles were analyzed using a power-law kinetic model of Mulla et al. [12b] developed for Pt/Al_2O_3 catalysts. We applied the Mulla model to our catalysts assuming first-order dependence in O_2 and NO partial pressures and negative first-order dependence in NO_2 partial pressure – orders close to those measured experimentally both by Mulla et al. [12b] and by Weiss and Iglesia [12c]. This allowed calculation of turnover rate, TOR (mol NO reacted)(mol surface Pt)$^{-1}$ s^{-1}), and apparent activation energy (kJ/mol) for comparison to other studies. The Mulla model also includes an approach-to-equilibrium term, β that was used to extract the forward reaction rate from the conversion (at a specific temperature) via an analytical solution of the plug-flow reactor equation assuming constant O_2 pressure. We limited our consideration of turnover rate to reaction conditions for which $\beta \leqslant 0.006$, focusing on rate comparisons at 150 °C.

Given the packed bed reactor configuration, external phase mass transfer limitations are not expected, nor are intra-particle diffusional limitations expected given the small particle size (<0.044 mm). Furthermore, Damkohler number calculations yielded values well below 1 for all but the highest temperature conditions approaching equilibrium conversions. Thus the rate of axial gas convection through the reactor was much greater than the reaction rate, and the measured reaction rates under consideration were not controlled by residence time.

3. Results

3.1. Microscopy results – AcAc catalysts

3.1.1. ACEM imaging of fresh AcAc catalysts

Aberration-corrected electron microscopy (ACEM) was used to determine the particle size and morphology of fresh AcAc catalysts. Typical HA-ADF images of the Pt50–Pd50 sample are shown in Fig. 1. In HA-ADF imaging, image contrast results primarily from differences in the atomic mass, and thus in these images, the brightest particles are the precious metals, the less bright regions are the γ-Al_2O_3 support, and the darkest areas are carbon-coated copper grids or vacuum.

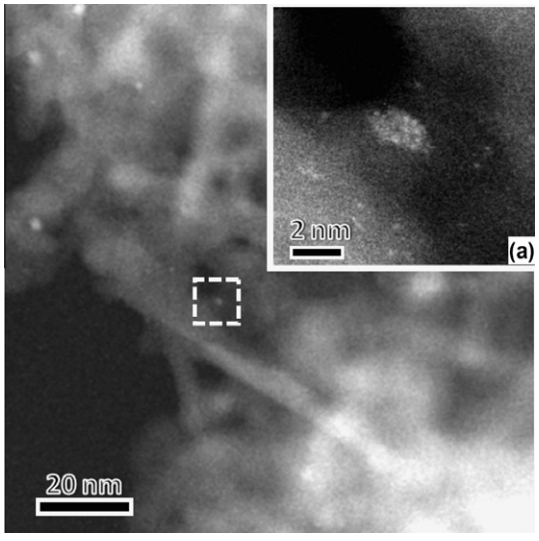

Fig. 1. Representative ACEM HA-ADF image of the fresh Pt50–Pd50 AcAc catalyst sample. Insert (a) is the highlighted area showing a 2 nm metallic cluster surrounded by atomically-dispersed metal.

Typical HA-ADF and bright field (BF) STEM images for the Pt100–Pd0 and the Pt50–Pd50 samples are shown in Fig. 2. In the Pt100–Pd0 HA-ADF image (Fig. 2a), one large ($d \sim 4$ nm) particle and several smaller Pt clusters are visible. In the corresponding BF image (Fig. 2b), only the large Pt particle is clearly evident. For the Pt50–Pd50 sample, small clusters of metal are visible in HA-ADF images (Fig. 2c) but not in BF imaging (Fig. 2d).

A notable feature of the Pt50–Pd50 samples is the appearance of regions where the precious metal is very highly dispersed, either as single atoms or clusters of atoms. The visibility of these sub-nanometer features, shown in Figs. 1a and 2c, demonstrates the importance of aberration-corrected HA-ADF imaging, as these features cannot be resolved in conventional HRTEM. Previous studies of supported precious-metal catalysts using the JEOL 2200FS ACEM have identified single atoms [13], as well as atomic "rafts" – 2-D clusters that do not display coherent crystallinity. That these smaller clusters do not appear in BF imaging provides further evidence of their lack of crystalline nature. (Note that in BF imaging, contrast comes primarily from diffraction; non-crystalline clusters thus lack the long-range order needed to diffract.) Intensity profile plots acquired across bright features in these clusters signify the presence of single atoms. In the HA-ADF STEM image shown in Fig. 3, for example, the dimensions of the features, as defined by the FWHM's of the intensity profiles measured across them, are comparable to reference values of single atomic diameters [14]. This supports the conclusion that these features are single precious metal atoms on the Al_2O_3 support. It should be noted that atomically dispersed Pt atoms are not prevalent in the Pt100–Pd0 sample, although 2-D "rafts" were visible in HA-ADF STEM imaging (Fig. 2a).

HA-ADF STEM imaging may also provide an indication of the chemical composition of these atomically dispersed species, which generally exhibit one of two relative intensity levels when comparably disposed (i.e., the species are not widely separated). For the feature indicated as "A" in Fig. 3, for example, the difference in intensity between the feature and the alumina support is approximately 50×10^4, while for the other feature (indicated as "B"), this difference is approximately 30×10^4. Assuming that "A" is Pt and "B" is Pd and that these numbers follow the expected trend, i.e., that contrast varies with $Z^{1.5-2}$ in HA-ADF imaging [15,16], the ratio of intensities should fall within the range 2.2–2.9. The discrepancy in this instance could be due to a difference in the amount of catalyst material, primarily alumina, between each of these particles and the electron source (more in the case of "A"). Intensity ratios of somewhat more than 2 were observed for other examples.

ACEM imaging was used to produce 3-D particle (i.e., excluding single atoms or 2-D rafts) size distributions, as shown in Fig. 4. The shapes of the distributions are quite similar, but the Pt100–Pd0 extends to larger particle size. (Note that the largest of these particles are larger than what we previously reported [3]. We ascribe this difference to the better discrimination that is possible with STEM.) The mean metal particle size for the Pt100–Pd0 and the Pt50–Pd50 catalysts are 1.27 and 1.03 nm, respectively. Although this difference is small, statistical analysis (a simple *t*-test) indicates that the observed difference in the means of the two samples is significant (*P* value = 0.00856). Particle size distribution statistics are listed in Table 2.

3.1.2. Imaging of Aged AcAc catalysts

Particle size distributions for the aged AcAc catalysts were originally collected using a JEOL 3011 HRTEM and presented in the previous study [3]. A summary of these results is reviewed later in Section 3.2.2.

3.1.3. Compositional analysis of AcAc catalysts

STEM imaging along with EDS analysis was performed on individual 3-D particles from Pt50–Pd50 samples in the fresh condition

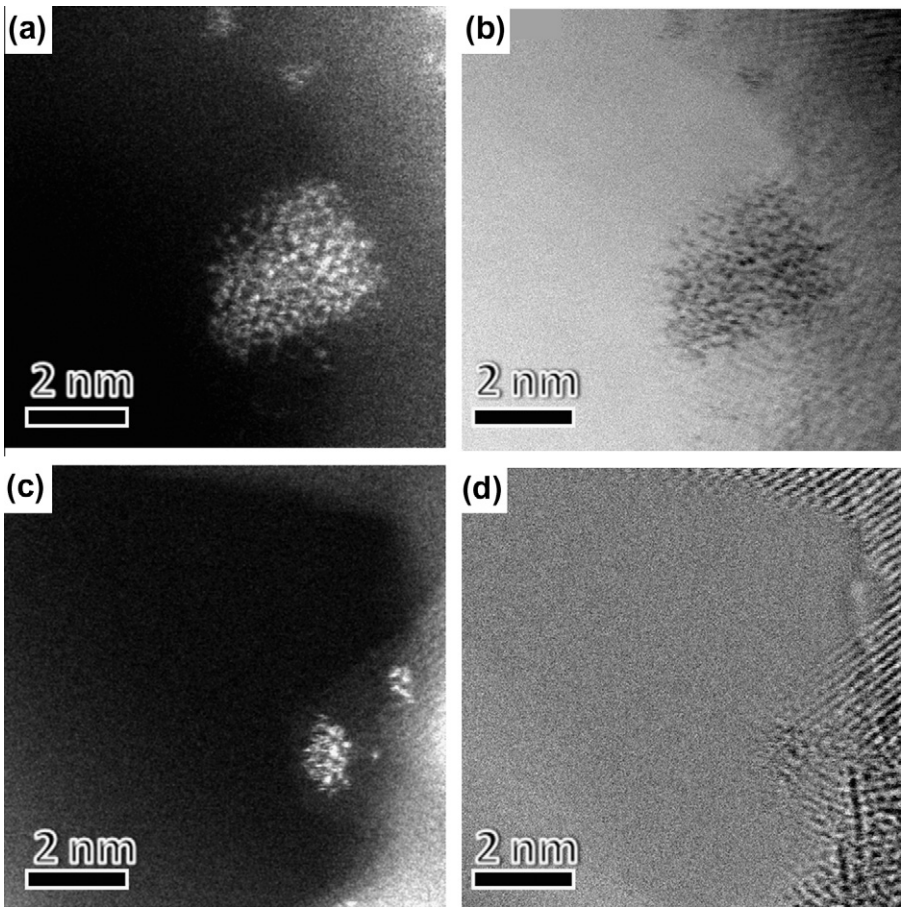

Fig. 2. (a) HA-ADF and (b) BF STEM images of typical particles in the fresh Pt100–Pd0 AcAc catalyst. (c) HA-ADF and (d) BF STEM images of typical particles in the fresh Pt50–Pd50 AcAc catalyst.

and after both aging treatments. For the fresh catalysts, instability under electron beam exposure prevented us from obtaining quantitative EDS on any but the largest six particles, which were clearly Pt-rich (averaging 86% Pt). However, quantitative EDS over a large area gave a composition close to the nominal value.

The compositions of individual particles for the two aging conditions are compared in Fig. 5. Catalyst particles tend to be Pt-rich after 500 °C aging (unfilled triangles in Fig. 5c), but after aging at 900 °C (unfilled squares in Fig. 5c), the composition of the catalyst particles converge to the nominal composition. From this plot, we conclude that both particle growth and alloying occur simultaneously during aging.

3.2. Microscopy results – Nitrate catalysts

3.2.1. ACEM imaging of fresh Nitrate catalysts

Typical ACEM BF and HA-ADF STEM images of fresh Pt100–Pd0 and Pt50–Pd50 catalysts made from nitrate precursors are shown in Fig. 6. Several small Pt clusters are clearly visible in the HA-ADF image of the Pt100–Pd0 catalyst (Fig. 6a), but they are only faintly visible in the corresponding BF image (Fig. 6b). For the Pt50–Pd50 sample, one large ($d \approx 8.5$ nm) metallic particle with clear lattice fringes is visible in both HA-ADF (Fig. 6c) and BF (Fig. 6d) imaging. This particle is surrounded by smaller clusters that are quite visible in HA-ADF (Fig. 6c), though not in BF imaging. The fast Fourier transform (FFT) of the BF image from the large particle (inset of Fig. 6d), indicates a plane spacing of 0.225 nm, in agreement with the expected spacing of the Pd (1 1 1) planes [17]. The atomically-dispersed metal seen in the Pt50–Pd50 AcAc sample (Fig. 1) is conspicuously absent in samples made from nitrate precursors. Although this could simply be a consequence of differences in the interaction chemistry of the two precursors with the alumina support, it should also be noted that the Nitrate catalysts were calcined in 20% O_2 vs. 5% O_2 for the AcAc catalysts. Pt particle sintering is known to increase with higher O_2 concentrations [1].

As was the case for samples of AcAc catalysts, aberration-corrected microscopy was used to obtain the distribution of 3-D particle sizes. Histograms comparing the particle size distributions for both compositions are shown in Fig. 7 (gray bars). The distributions obtained from AcAc catalysts (white bars) are overlaid for comparison. The most significant difference among all the samples is that the Pt50–Pd50 Nitrate catalyst has a notably larger mean particle size (Table 2), due to the presence of a significant number of much larger particles.

3.2.2. Imaging of aged Nitrate catalysts

Results from TEM particle size measurements of the aged Nitrate catalysts are summarized in Fig. 8, along with previous results from aged AcAc catalysts, for comparison. Regardless of the aging temperature, the Pt100–Pd0 AcAc catalysts have a somewhat larger mean particle size than the corresponding Nitrate catalysts (Table 2), possibly arising from the small difference in particle size distributions of the fresh catalysts (Figs. 4a vs. 7a and Table 2). In the case of the Pt50–Pd50 composition, the presence of a significant number of large particles in the fresh Nitrate catalyst is most likely responsible for the larger (relative to the AcAc catalyst) mean particle sizes after aging, especially at 500 °C. After aging at 900 °C,

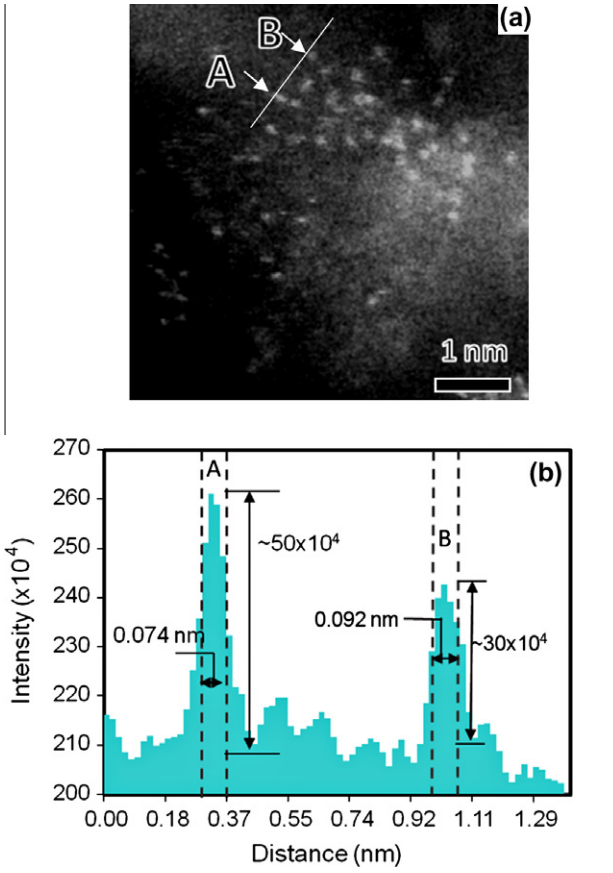

Fig. 3. (a) High resolution ACEM HA-ADF image of a cluster of atomically dispersed atoms in the fresh Pt50–Pd50 AcAc catalyst. The breadths of the intensity line scan in (b) suggest that these particles are single atoms of (A) platinum and (B) palladium.

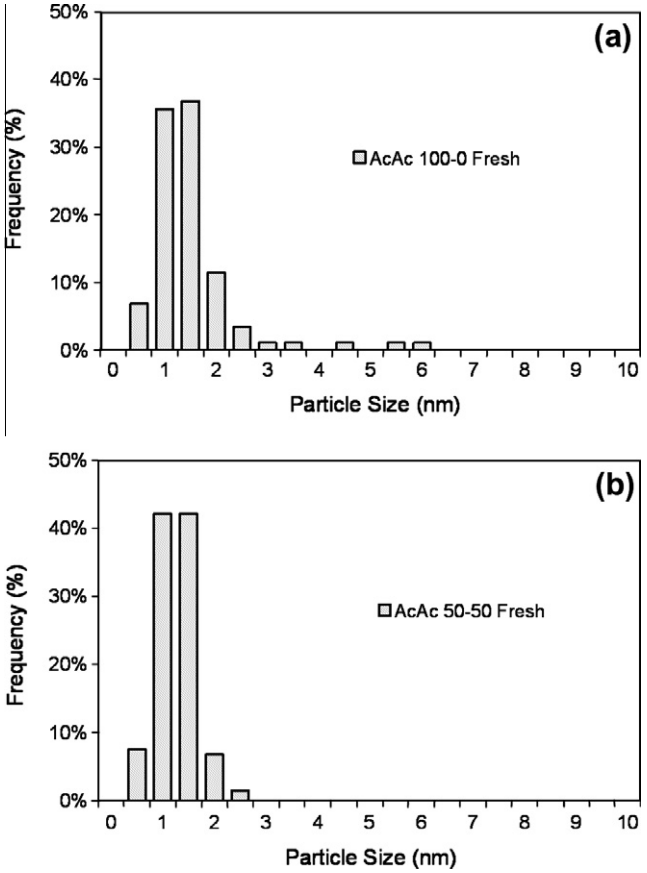

Fig. 4. 3-D particle size distributions of fresh (a) Pt100–Pd0 and (b) Pt50–Pd50 AcAc catalysts collected from ACEM HA-ADF imaging.

the Pt50–Pd50 catalysts had a smaller mean particle size than the Pt100–Pd0 catalysts for both precursors, primarily due to the absence of anomalously large particles (ALPs) of Pt (particles with $d > 100$ nm, as typified by the large separation between mean and maximum values in Fig. 8 and Table 2). Examples of such ALPs, typically highly faceted, some of which were clearly not spherical, are shown in Fig. 9a and b. Regardless of precursor used, the addition of Pd appeared to suppress the growth of these particles, as illustrated by the image shown in Fig. 9c, obtained from the 900 °C aged Nitrate catalyst.

Surface-weighted mean diameters and dispersions (expressed in %) were calculated according to Eqs. (1) and (2) above and are presented in Table 2 along with other statistics obtained from the TEM measurements. As expected, the dispersion generally follows an inverse relationship to mean particle size. For all samples, dispersion decreased with aging due to particle growth, though bimetallic catalyst particles grew less than pure Pt catalyst particles, resulting in a somewhat less severe decrease in dispersion. The unexpected relative dispersions of the Pt100–Pd0 and Pt50–Pd50 Nitrate catalysts after 500 °C aging are likely a consequence of the unusually wide particle size distribution measured for the fresh Pt50–Pd50 catalyst (Fig. 7b), the nature of which is described in Section 3.2.3.

3.2.3. Compositional analysis of Nitrate catalysts

STEM imaging with EDS analysis was also performed on individual particles in catalysts made from the nitrate precursor. For the fresh Pt50–Pd50 sample, the average 3-D particle composition was 42% Pd. However, the Pd was distributed bi-modally (Fig. 10), with small ($d < 3$ nm) particles biased to Pt-rich and larger particles (in the 3–11 nm size range) biased to Pd-rich.

The compositions of individual particles in Pt50–Pd50 Nitrate catalysts after aging are compared in Fig. 11. While aging at 500 °C (Fig. 11c, filled triangles) induced particle growth, the distribution retained most of the bimodal nature evident in the fresh state. After aging at 900 °C (filled squares), the compositions of the particles were much more tightly distributed around the nominal alloy composition. The effect of the difference in initial state between the Pt50–Pd50 Nitrate and AcAc catalysts on subsequent changes in particle size and composition induced by aging is clearest in the 500 °C case. Thus, while particle growth and alloying again appear to occur simultaneously in the Pt50–Pd50 Nitrate catalyst, the apparent influence of Pd on particle growth (inhibition) at 500 °C is less than in the corresponding AcAc catalyst.

3.3. XRD results

XRD data for the Nitrate catalysts were collected to further investigate crystallite size and lattice parameter. A comparison of the crystallite sizes for each aged Nitrate catalyst is shown in Table 3. Clearly, the Pt100–Pd0 catalyst experiences much more metal particle growth at 900 °C than the Pt50–Pd50 catalyst. Additionally, the Pt100–Pd0 crystallites appear to be significantly larger than the Pt50–Pd50 crystallites after aging at only 500 °C, a result that is not consistent with the TEM finding (Table 2).

A comparison of the lattice parameters obtained by fitting the peak positions was also performed, and as expected, the aged Pt100–Pd0 catalysts have lattice parameters that closely correspond to the value expected for bulk Pt ($\alpha_{Pt} = 3.92$ Å [18]) while

Table 2
Summary of TEM-derived 3-D particle size statistics. Fresh catalysts were measured using HA-ADF STEM imaging in the JEOL 2200FS while aged catalysts were measured using BF TEM imaging on the JEOL 3011 microscope. Dispersion, derived using Eqs. (1) and (2) but expressed in%, may be roughly compared with the CO/M value (ratio of the number of chemisorbed CO to number of metal atoms in the sample), taken from Ref. [3], by assuming an adsorption stoichiometry of about 1 and multiplying the CO/M value by 100.

Sample	Counts	Mean (nm)	Std. dev (nm)	Min (nm)	Max (nm)	d_s (nm)	Dispersion D (%)	CO/M from [3]
Pt100–Pd0 fresh (AcAc)	87	1.27	0.89	0.18	5.68	2.95	38.0	0.668
Pt50–Pd50 fresh (AcAc)	133	1.03	0.38	0.08	2.03	1.27	88.5	0.456
Pt100–Pd0 500 °C (AcAc)	109	9.04	3.01	2.80	19.4	10.9	10.3	0.184
Pt50–Pd50 500 °C (AcAc)	101	4.90	1.26	2.61	8.57	5.55	20.3	0.182
Pt100–Pd0 900 °C (AcAc)	100	60.5	70.4	5.06	501	277	0.41	0.007
Pt50–Pd50 900 °C (AcAc)	103	22.1	14.5	2.48	63.8	38.2	2.95	0.014
Pt100–Pd0 fresh (Nitrate)	125	1.38	0.50	0.12	2.78	1.74	64.6	–
Pt50–Pd50 fresh (Nitrate)	127	2.79	2.62	0.08	14.9	7.87	14.3	–
Pt100–Pd0 500 °C (Nitrate)	215	6.15	1.58	2.39	10.1	7.52	14.9	–
Pt50–Pd50 500 °C (Nitrate)	159	7.58	2.32	2.05	15.3	8.86	12.7	–
Pt100–Pd0 900 °C (Nitrate)	227	43.4	48.6	7.84	527	146	0.77	–
Pt50–Pd50 900 °C (Nitrate)	108	28.2	11.5	5.38	71.7	37.0	3.04	–

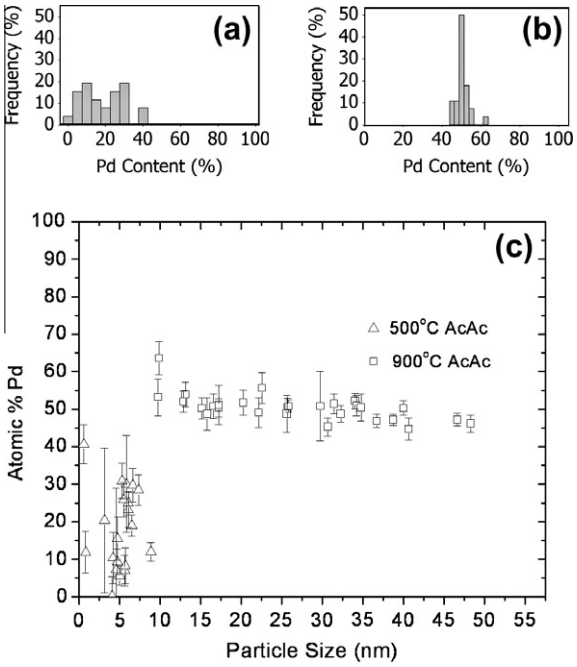

Fig. 5. The compositional distributions of Pt50–Pd50 AcAc catalysts aged at 500 °C (a) and 900 °C (b), together with their particle compositions plotted as a function of 3-D particle size (c). The error bars represent the Pd compositional measurement uncertainty from the EDS integration.

the aged Pt50–Pd50 catalysts both yield lattice parameters very close to the average value for a 50:50 alloy of Pt and Pd. In the case of the catalyst aged at 900 °C, this is expected because Pt–Pd alloys deviate only slightly from Vegard's Law [19]. In the case of the catalyst aged at 500 °C, however, it could reflect an averaging over particles of varying composition, ranging from Pt-rich to Pd-rich, as revealed in the EDS compositional analysis (Fig. 11c). The inconsistency in crystallite size noted above could thus be a consequence of inhomogeneous broadening.

3.4. Catalytic performance

NO oxidation activity data were collected for both Nitrate (this study) and AcAc (previous study [3]) catalysts in our multichannel flow reactor. The NO conversion profiles are shown as a function of temperature for the Pt100–Pd0 and Pt50–Pd50 catalysts in Fig. 12a and b, respectively. The general shape of these oxidation activity plots is dictated by the kinetics of the NO oxidation reaction at low temperatures and the thermodynamic equilibrium between NO and NO_2 at high temperatures. For both precursors and metal compositions, we see that 500 °C aged catalysts are more active than those aged at 900 °C, which themselves are more active than the fresh catalysts.

NO Activity : 500 °C Aged > 900 °C Aged > Fresh

This ordering of activities is consistent with the known structure sensitivity of the NO oxidation reaction, where very small Pt particles have intrinsically low activities, and harshly aged catalysts suffer from low overall Pt surface area [20a,12b,12c]. For the purpose of comparing the activities of the catalysts, the conversion at 150 °C is plotted as a function of dispersion derived from the TEM-measured particle size (Table 2) in Fig. 13. The NO oxidation data are also reported in Table 4 on both a rate per g-cat basis at 150 °C using a kinetic analysis reported previously [3] and as a turnover rate (TOR) calculated using the rate expression of Mulla et al. [12b] as described in the experimental section. Most notable in both the conversion and rate data is the much lower activity of the fresh AcAc than Nitrate catalyst for both Pt100–Pd0 and Pt50–Pd50. Differences in the fresh AcAc vs. Nitrate NO oxidation activities notwithstanding, the activity data after aging at 500 and 900 °C are relatively close for the two precursors, based on both measured rate and calculated TOR.

Catalyst composition also had a relatively minor effect on the mass-based rates for each precursor at each level of aging, except for the fresh Nitrate catalysts where the rate over the Pt100–Pd0 catalyst was twice that of the Pt50–Pd50 catalyst (Table 4). Turnover rates (also given in Table 4) showed the opposite trend (i.e., TOR of the Pt50–Pd50 catalyst was 1.5 times that of the Pt100–Pd0 catalyst). The NO oxidation reaction on Pt catalysts is structure sensitive with larger particle having higher TOR [12b]. Thus, on a TOR basis, the Pt50–Pd50 catalyst (D = 14.3%) would be expected to have a much higher TOR than the Pt100–Pd0 catalyst (D = 64.6%). In fact, aging the Pt50–Pd50 catalyst at 500 °C retained nearly identical dispersion (12.7% vs. 14.3%) but increased the TOR 3.6 times. These results can only be understood from the compositional analysis afforded by STEM with EDS. Both the low mass-based rate and unexpectedly low TOR of the fresh Pt50–Pd50 Nitrate catalyst are consistent with Fig. 10, where it is clear that a significant amount of the Pt in the Pt50–Pd50 catalyst is associated with large Pd-rich particles that likely have low NO oxidation activity. In comparison, the fresh Pt100–Pd0 Nitrate catalyst has a lower TOR because of its very small particle size, but it has much more Pt surface area, thereby explaining its higher mass-based rate. From Fig. 11 it is also clear that the average particle size of the Pt50–Pd50 catalyst does not grow significantly upon aging at 500 °C, but the particle composition distribution becomes less

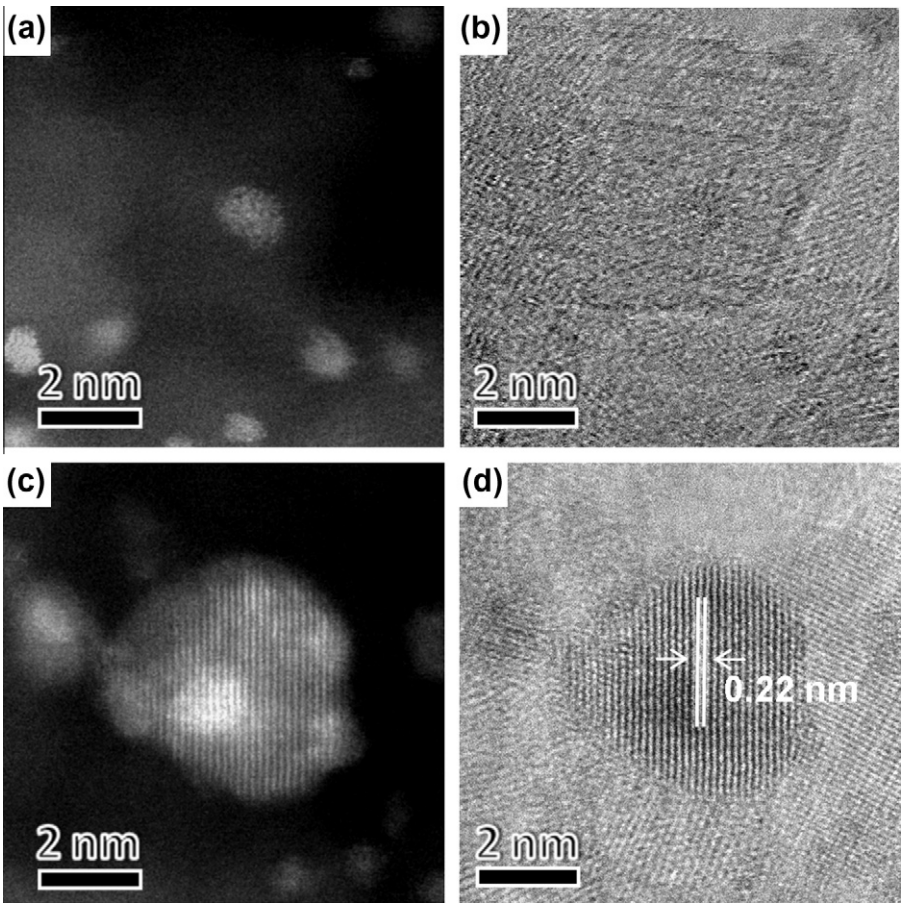

Fig. 6. (a) HA-ADF and (b) BF STEM images from the fresh Pt100–Pd0 Nitrate catalyst. (c) HA-ADF and (d) BF STEM images from the fresh Pt50–Pd50 Nitrate catalyst.

bimodal, with a shift of the Pt-rich particles to larger size and greater Pd content at the expense of the larger Pd-rich particles in the fresh catalyst.

The other notable difference between the Pt50–Pd50 and Pt100–Pd0 counterpart catalysts, for both Nitrate and AcAc precursors, are the much greater TORs for the 900 °C aged Pt100–Pd0 catalysts, despite relatively similar mass-based rates. This is due to the ALPs in the Pt100–Pd0 catalysts. The Pt50–Pd50 catalysts have more surface sites (i.e., lower TORs) but the Pt100–Pd0 catalysts have larger particles on average (see Fig. 8) which translates to higher rates per particle because of the structure sensitive nature of the reaction. Hence, the mass-based rates are nearly identical.

4. Discussion

Analytical electron microscopy, involving STEM coupled with EDS and HA-ADF imaging, has been widely used to investigate structure and composition of bimetallic catalysts since the pioneering work of Lyman and co-workers on the Pt–Rh system more than a decade ago [20b]. In the present work, our further application of advanced electron microscopy techniques, especially ACEM for imaging very small features and HA-ADF imaging coupled with EDS for compositional analysis of small particles, has provided new and useful information about the Pt and Pt–Pd catalysts prepared for our previous study of the effects of alloying on dispersion stability and performance of NO oxidation catalysts [3]. Our new observations reveal subtle, but significant differences in the initial metal distributions that can reasonably be related to catalyst synthesis. Previous work has suggested a tendency for platinum(II) and palladium(II) bis-acetylacetonates dissolved in acetone to become associated into bimetallic complexes in solution [4,21], leading to a high degree of Pt–Pd association in a freshly-prepared bimetallic catalyst. In our earlier study, we found a substantial difference in the efficiency of adsorption of the single-metal acetylacetonate precursors from solution onto the alumina support, Pt adsorption being much more limited than Pd. Assuming that the higher efficiency of Pd adsorption could be imparted, to some degree, to the bimetallic complex in solution, it would not be surprising to find a somewhat higher dispersion in the case of the Pt50–Pd50 than the Pt100–Pd0 catalyst. The presence of larger particles in the fresh Pt100–Pd0 catalyst (Fig. 4) is consistent with this expectation, but an even more significant piece of supporting evidence is the qualitative observation that more atomically-dispersed features (e.g., Figs. 2c and 3) appear in the Pt50–Pd50 than the Pt100–Pd0 catalyst. The relatively high CO/M value (ratio of the number of chemisorbed CO to the number of metal atoms in the sample) for the fresh AcAc Pt100–Pd0 catalyst (0.668) in contrast to the TEM-based dispersion of 38% may also be consistent with the observation of raft-like structures in the fresh AcAc sample – not included in the 3-D particle statistics of Table 2, but likely contributing to the CO/M measurement. ACEM observations made on fresh Pt0–Pd100 (i.e., pure Pd) AcAc catalyst samples [22] also revealed the presence of more atomically-dispersed metal features than in the corresponding Pt100–Pd0 catalyst, though contrast was relatively poor in this case.

Spectroscopic (*via* EDS) determination of the amount of Pt and Pd in all of the individual metal particles in the fresh Pt50–Pd50 catalyst was still beyond our reach, though area-averaged results

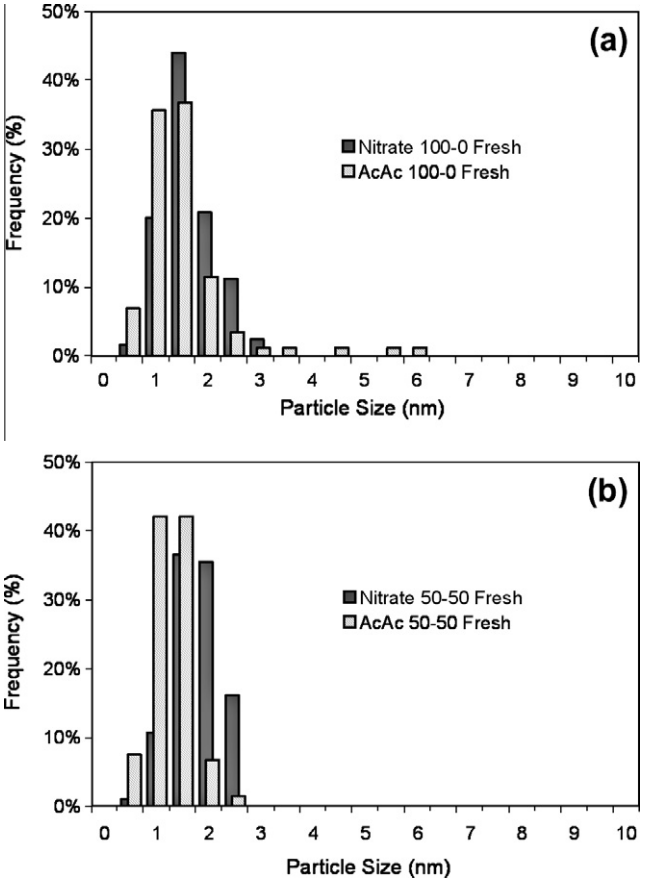

Fig. 7. 3-D particle size distributions collected from STEM imaging of fresh (a) Pt100–Pd0 and (b) Pt50–Pd50 catalysts. White bars represent AcAc catalysts, gray bars represent Nitrate catalysts.

suggest that much of the Pd in the fresh catalyst may be more highly dispersed than Pt and thus that the two metals are generally not in close association with each other. Indeed, the compositional measurement of metal particles after aging at 500 °C reveals that they are Pt-rich (Fig. 5). The missing Pd is likely still highly dispersed, reflecting a relatively immobile oxidized (while aging)

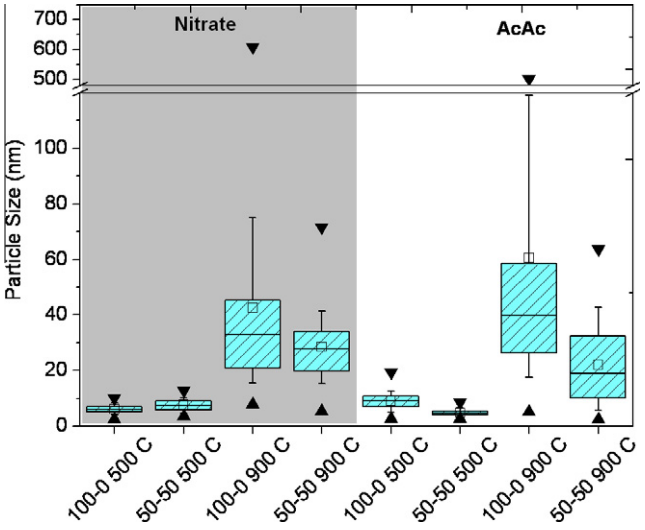

Fig. 8. Box-plot summarizing descriptive statistics of the aged Nitrate and AcAc catalysts. Boxes represent the inter-quartile range, whiskers represent 5th and 95th percentile, ▼ represents the maximum values, ▲ represents the minimum values, – represents the median values, and □ represents the arithmetic means.

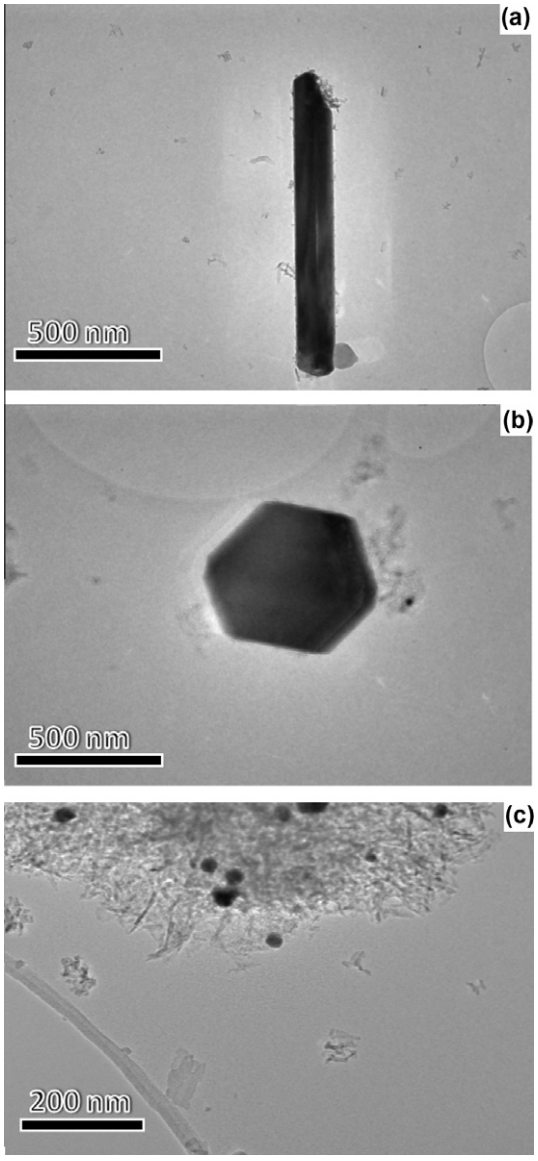

Fig. 9. (a) TEM image of a Pt needle found in the Pt100–Pd0 Nitrate catalyst aged at 900 °C. (b) Highly faceted Pt particle from the same catalyst sample shown in (a) (Structures like these were noticeable features of the Pt100–Pd0 samples aged at 900 °C from both catalyst precursors.) (c) TEM image of metallic particles in the Pt50–Pd50 Nitrate catalyst aged at 900 °C.

form [3]. Eventually, though, all of the Pd becomes incorporated into the initially Pt-rich particles after aging at 900 °C. As we demonstrated previously, the degree to which addition of Pd inhibits particle growth increases with Pd concentration, but since the actual amount of Pd in the bimetallic particles at intermediate stages of aging appears to be varying with exposure to lean conditions, experiments aimed at probing the correlation between particle composition and size as a function of time at fixed aging temperatures are needed in order to sort out the precise dependence. The mechanism (or mechanisms) by which particle growth inhibition occurs is (are) still unknown, but our HA-ADF imaging with EDS is not consistent with the suggestion that a thick (>2 nm) surface layer of PdO (or Pd) simply protects Pt from direct exposure to O_2. (Previous experimental [23,24] and theoretical [25,26a] reports have suggested that a core–shell segregation of Pt and Pd can occur under certain conditions.) Further illumination of this issue may be possible with the recent development of specialized EDS detectors that have been optimized for aberration-corrected microscopes.

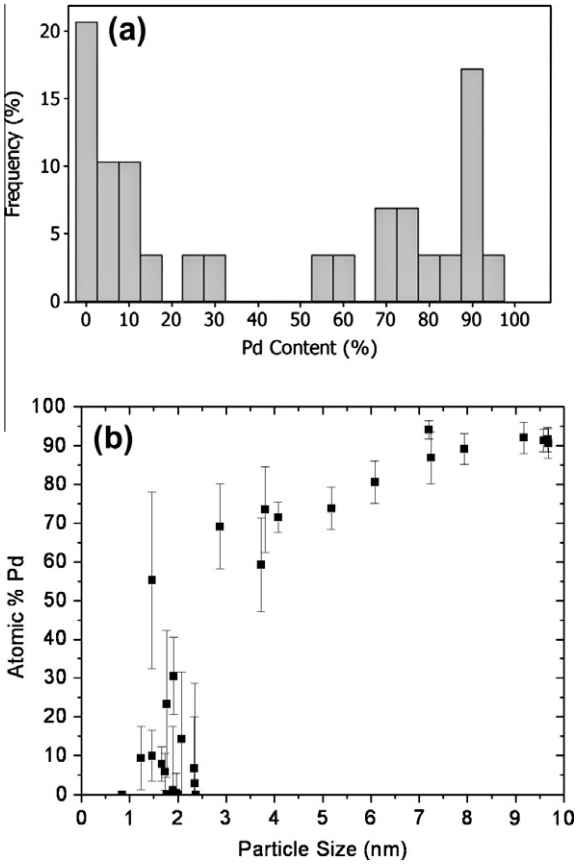

Fig. 10. (a) Compositional distribution of fresh Pt50–Pd50 Nitrate catalyst, and (b) the particle composition plotted as a function of 3-D particle size. The error bars represent the Pd compositional measurement uncertainty from the EDS integration.

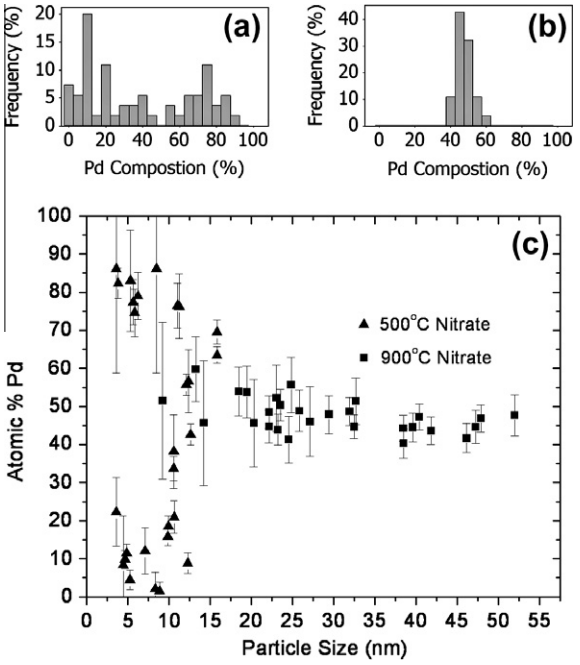

Fig. 11. The compositional distributions of Pt50–Pd50 Nitrate catalysts aged at 500 °C (a) and 900 °C (b), together with their particle compositions plotted as a function of 3-D particle size (c). The error bars represent the Pd compositional measurement uncertainty from the EDS integration.

Table 3
XRD crystallite sizes obtained by a Scherrer analysis of (3 1 1) profiles for catalysts prepared from nitrate solutions.

Aging temperature (°C)	Crystallite size (nm)	
	Pt100–Pd0	Pt50–Pd50
500	23	8
900	62	20

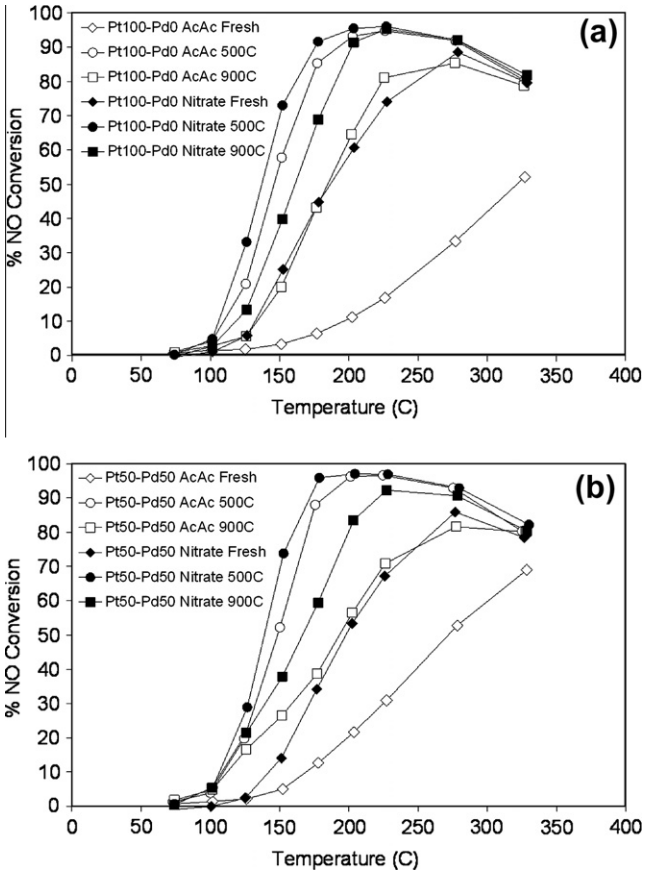

Fig. 12. NO conversion curves for (a) Pt100–Pd0 catalysts and (b) Pt50–Pd50 catalysts.

These tools have been used to provide atomic scale compositional information about the nanoparticles in a variety of multi-metallic catalysts including Au–Pd and Au–Ag [26b] and Pd–Fe–Pt [26c].

The newly-prepared set of Pt and Pt–Pd catalysts, made with nitrate precursors, provide a number of interesting points of contrast with the AcAc catalysts. Starting with the fresh catalysts, a large reversal in the relative dispersions of the two catalyst compositions was observed (Table 2), due to the formation of fairly large (3–10 nm) Pd-rich particles (the compositions of which could be measured by EDS) in the Pt50–Pd50 catalyst. This circumstance, which itself is not believed to be of fundamental significance, creates a situation in which the change in both particle size and composition can be determined upon aging at 500 °C, as shown in Fig. 11. As might be expected, both the Pd-rich and Pt-rich particles grow, and the composition range shrinks. A substantial number of large, Pd-rich particles, not found in the corresponding AcAc catalyst, are present after aging at 500 °C. Never-the-less, after aging at 900 °C, a fairly narrow range of particle compositions, centered at the nominal value, was observed, just as in the case of the Pt50–Pd50 AcAc catalyst.

Evolution of the Pt100–Pd0 Nitrate catalyst was quite similar to that of the corresponding AcAc catalyst, as expected in view

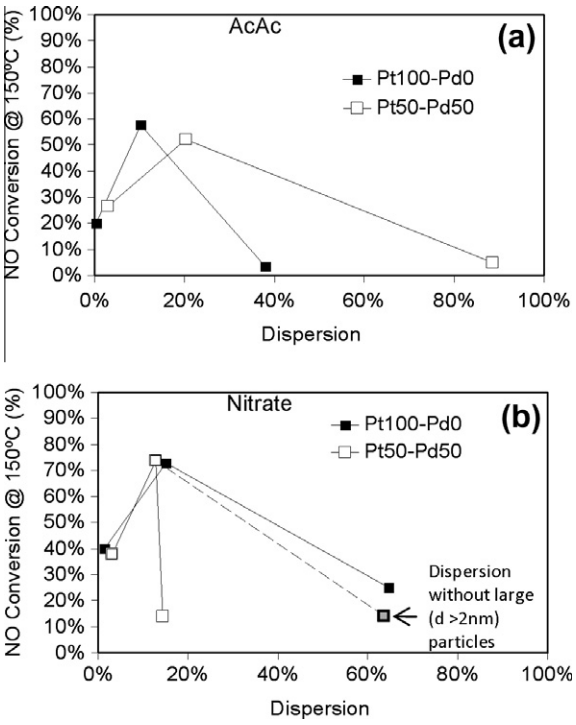

Fig. 13. NO conversion at 150 °C plotted as a function of particle size for AcAc catalysts (a) and Nitrate catalysts (b). Pure Pt catalysts are shown with solid squares, and bimetallic catalysts with open squares. The gray symbol in (b) represents the dispersion calculated without including large Pd-rich particles, which presumably do not contribute significantly in NO conversion.

Table 4
NO oxidation rate data.

Catalyst description	Rate at 150 °C (μmol/gcat s) [TOR ($\times 10^{-2}$) (s^{-1})][a]	
	Nitrate	AcAc
Pt50–Pd50 fresh	2.2 [0.26]	0.84 [0.015]
Pt50–Pd50 500 °C	6.0 [0.87]	6.0 [0.51]
Pt50–Pd50 900 °C	5.1 [2.73]	3.9 [2.1]
Pt100–Pd0 fresh	4.7 [0.16]	0.71 [0.028]
Pt100–Pd0 500 °C	7.6 [0.94]	7.8 [1.32]
Pt100–Pd0 900 °C	6.6 [14]	3.8 [14.9]

NB – The surface Pd atoms are not included in the calculated TOR for Pt50–Pd50.
[a] (mol NO reacted)(mol surface Pt)$^{-1}$ s^{-1}, calculated as explained in the text.

of the similarity of their initial states. In neither case was there evidence for large particles in the fresh catalyst that could have seeded the growth of the ALPs. This suggests that the presence of ALPs in the aged catalysts is more a consequence of the growth mode than the initial particle size distribution. The presence of these particles is consistent with earlier studies that identified bi-pyramids, multiply-twinned particles, rods, and plate-like particles in alumina-supported Pt catalysts after both laboratory and vehicle aging conditions [27,28].

Much effort has been devoted to using particle size distributions to identify particle growth mechanisms in the past [29]. In this study, particle size distributions after aging at 900 °C closely fit the log normal distribution function, which suggests that the dominant sintering mechanism is particle migration and coalescence [29,30a]. However, the presence of the highly faceted ALPs is not consistent with a migration and coalescence growth model. In an early report on the sintering of alumina-supported Pt, Harris et al. [28] found migration and coalescence was the dominant growth mode for short sintering times, while growth of ALPs at longer sintering times was mediated by inter-particle transport. Relative to the current study, the role of Pd in inhibiting Pt particle growth, primarily through the suppression of ALP formation, may thus be linked to its effect on inter-particle transport of Pt.

The NO oxidation performance of both sets of catalysts (Fig. 12) are generally comparable and in reasonable agreement with the structure sensitive nature of the NO oxidation reaction on Pt/Al_2O_3 catalysts. Although a detailed kinetic study was not the focus of our work, analysis of turnover rates based on the kinetic model of Mulla et al. [12b] showed a progressive increase in TOR for all catalysts with extent of aging, despite the eventual downturn in the mass-based rates for the 900 °C catalysts due to loss of surface Pt sites dominating over the continued increase in site-specific NO oxidation rate with increasing particle size (Table 4 and Fig. 13). The increase in conversion with 500 °C aging is especially dramatic in the case of the Pt50–Pd50 nitrate catalyst, in spite of the fact that its apparent dispersion was relatively low in the fresh state (14.3%) and didn't change much (to 12.7%) upon aging, as shown in Table 2. Considering the Pd concentration as a function of particle size (Fig. 10), however, it is evident that there is a critical size (~2.5 nm) below which the particles are Pt-rich and above which the particles are Pd-rich. If one does not consider the Pd-rich particles, which are expected to have low intrinsic activity, the initial dispersion is about 64%, and the trends in Fig. 13b are more consistent with those of the pure Pt catalyst (as shown by the dashed line and solid square symbol). We note that the apparent activation energies we calculated for the Pt100–Pd0 Nitrate catalysts using the low temperature (⩽150 °C) TORs obtained from the Mulla model analysis are larger, and the values of TOR themselves are much larger than those typically reported in the literature when extrapolated to our conditions. For example, extrapolating the Mulla et al. TOR of 1.5×10^{-2} s^{-1} for a sintered catalyst (7 nm Pt particle size) at 300 °C, 10% O_2, 300 ppm NO, 170 ppm NO_2 [12b], to our conditions (125 °C, 8% O_2, 333 ppm NO, 167 ppm NO_2) for the 500 °C aged Nitrate catalyst (7.5 nm Pt particle size) yielded a TOR of 7.5×10^{-6} s^{-1}, compared with our calculated TOR of 6.7×10^{-3} s^{-1}. Part of this discrepancy could be the much different conditions under which our experiments were run (i.e., lower temperatures, lower space velocities (to produce higher conversions) and no NO_2 addition to the feed) and associated limitations of applying the Mulla kinetic model under conditions so far removed from where it was established. However, another reason for higher calculated TOR values in our study could be the experimental procedure, which involved first reducing the catalyst and then gradually increasing the temperature in the reaction stream (no NO_2 in the feed) and collecting data at fixed temperatures. A number of studies have shown that exposure of Pt catalysts to NO_2 in particular decreases the NO oxidation activity with respect to catalysts that have not been pre-exposed to NO_2 [12b,30b]. We speculate that the conditions of the Mulla et al. experiments, which involved reaction at 300 °C with 170 ppm NO_2 in the feed, may have produced a less active state of their catalyst than in our experiments conducted mostly at lower temperatures, with catalyst pre-reduction, and without NO_2 in the feed.

There still remains the apparent question of the mechanism by which Pd alloying inhibits Pt particle growth without greatly affecting NO oxidation activity, especially given the much lower rates of NO oxidation reported on supported Pd/Al_2O_3 catalysts vs. Pt/Al_2O_3 catalysts over the optimal range of particle sizes observed in our study [31]. However, recently reported [32] first principles calculations of NO oxidation on meta-stable Pd surface oxide films (observed experimentally by Lundgren et al. [33]) have shown NO oxidation rates comparable to those reported for Pt, thus suggesting that surface PdO could have a similar

characteristic in supported Pt–Pd particles typical of our study. As mentioned earlier, no strong evidence of a thick (>2 nm) Pd or PdO shell protecting a Pt rich core was observed in this study; however, our characterization techniques would not have identified a monolayer type PdO surface film on the larger alloyed particles produced after 500 °C and 900 °C aging. Thus our present results do not contradict the possibility of an ultrathin meta-stable surface PdO film theoretically characterized by high NO oxidation activity.

The choice of precious metal precursor also did not have a strong effect on NO oxidation rate except for the fresh catalysts. As noted in Section 3.4, the roughly twofold larger rate observed at 150 °C for the fresh Nitrate catalyst may have resulted from the higher oxygen concentration utilized in calcining the nitrate samples and a corresponding increase in particle coarsening for those samples. Overall, the precious metal characterization data combined with the NO oxidation data suggest that the fresh AcAc catalysts contained more precious metal in the form of single atoms or raft-like structures that would be expected to have lower activity for the structure-sensitive NO oxidation reaction than coalesced 3-D particles.

From a practical standpoint, automotive exhaust applications requiring NO oxidation, such as diesel oxidation catalysts or catalyzed diesel particulate filters, operate for the most part in a temperature range closer to the mid-point temperature of 500 °C of this study than the fresh or 900 °C aged conditions. This study showed virtually no effect of precursor choice on NO oxidation rate after aging at the 500 °C condition and only about a 25% higher rate for the pure Pt catalysts vs. the Pt50–Pd50 catalysts despite the factor of two difference in Pt concentration. These observations further suggest that a pretreatment procedure involving calcination of Pt–Pd catalysts at 500 °C prior to use produces close to an optimum particle size distribution for NO oxidation (5–10 nm). Additionally, it is clear from the compositional data for the Pt–Pd catalysts in Figs. 5 (AcAc) and 11 (Nitrate) that 500 °C calcination also generates a high concentration of Pt-rich particles in the optimal size range. Similar benefits are reaped after the extreme temperature aging at 900 °C. In that case, rates are again roughly comparable for the pure Pt and Pt50–Pd50 catalysts, likely reflecting a trade-off between lower intrinsic activity of the fully alloyed bimetallic catalysts (compared to pure Pt at a given particle size) and loss of Pt surface area to anomalously large particles (in the case of the pure Pt catalysts).

5. Conclusions

Application of advanced electron microscopy techniques to the characterization of alumina-supported Pt and Pt–Pd catalysts has allowed us to refine our knowledge of the degree of alloying that exists at various stages of aging under lean conditions and thus better understand its relationship to particle coarsening. Although some direct association between Pt and Pd may be attained at the initial stage of bimetallic catalyst synthesis, there is clearly a strong tendency for alloying to proceed *in situ* during the course of lean aging, and this certainly has a positive influence on limiting the growth of anomalously large particles typically found in pure Pt catalysts that have been harshly aged under lean conditions.

We have also again demonstrated that replacement of moderate amounts of Pt with Pd can be done with little or no loss of overall NO oxidation activity. Further, standard catalyst precursors and synthesis methods have been shown to suffice; moreover, catalyst calcination at 500 °C has been shown to produce roughly optimal particle size for promoting the structure-sensitive NO oxidation reaction. These results provide fundamental understanding of the advantages associated with the use of Pd to both increase catalyst durability and decrease Pt loading in Pt-based catalysts for lean-burn engine exhaust-gas treatment. As is often the case, experience precedes detailed understanding; Pt–Pd bimetallic catalysts are already widely utilized in commercial diesel oxidation catalyst formulations for robust, cost-effective emissions control.

Acknowledgments

The authors would like to thank Joe Kazemi of The University of Michigan Center for Statistical Consultation and Research (CSCAR) for his assistance with statistical analysis.

The work at the University of Michigan was supported by the National Science Foundation under Grants DMR-0907191, CBET-0933239, and DMR-0723032. The research at the Oak Ridge National Laboratory's High Temperature Materials Laboratory was sponsored by the US Department of Energy, Office of Energy Efficiency and Renewable Energy, Vehicle Technologies Program.

References

[1] G.W. Graham, H.-W. Jen, W. Chun, H.P. Sun, X.Q. Pan, R.W. McCabe, Catal. Lett. 93 (2004) 129–134.
[2] M. Chen, L.D. Schmidt, J. Catal. 56 (1979) 198–218.
[3] G.W. Graham, H.W. Jen, O. Ezekoye, R.J. Kudla, W. Chun, X.Q. Pan, R.W. McCabe, Catal. Lett. 116 (2007) 1–8.
[4] F. Morfin, J.-C. Sabroux, A. Renouprez, Appl. Catal. B 47 (2004) 47–58.
[5] J.L. Rousset, B.C. Khanra, A.M. Cadrot, F.J.C.S. Aires, A.J. Renouprez, M. Pellarin, Investigations on supported bimetallic PdPt nanostructures, in: Surface Science Proceedings of the 15th European Conference on Surface Science, vol. 352–354, 1996, pp. 583–587.
[6] J. Hagen, Industrial Catalysis: A Practical Approach, second ed., Wiley-VCH, Weinheim, Germany, 2006.
[7] L.F. Allard, D.A. Blom, M.A. O'Keefe, C.J. Kiely, D. Ackland, M. Watanabe, M. Kawasaki, T. Kaneyama, H. Sawada, Microsc. Microanal. 10 (2004) 110–111.
[8] M.A. O'Keefe, L.F. Allard, D.A. Blom, J. Electron Microsc. (Tokoyo) 54 (2005) 169–180.
[9] G. Cliff, G.W. Lorimer, J. Microsc. – Oxford 103 (1975) 203–207.
[10] H.R. Aduriz, P. Bodnariuk, B. Coq, F. Figueras, J. Catal. 119 (1989) 97–107.
[11] M.M. Hall Jr., V.G. Veeraraghavan, H. Rubin, P.G. Winchell, J. Appl. Crystallogr. 10 (1977) 66–68.
[12] (a) P.J. Schmitz, R.J. Kudla, A.R. Drews, A.E. Chen, C.K. Lowe-Ma, R.W. McCabe, W.F. Schneider, C.T. Goralski Jr., Appl. Catal. B 67 (2006) 246–256;
(b) S.S. Mulla, N. Chen, L. Cumaranatunge, G.E. Blau, D.Y. Zemlyanov, W.N. Delgass, W.S. Epling, F.H. Ribeiro, J. Catal. 241 (2006) 389–399;
(c) B.M. Weiss, E. Iglesia, J. Phys. Chem. C 113 (2009) 13331–13340.
[13] J.H. Kwak, J.Z. Hu, D. Mei, C.W. Yi, D.H. Kim, C.H.F. Peden, L.F. Allard, J. Szanyi, Science 325 (2009) 1670–1673.
[14] L. Pauling, J. Am. Chem. Soc. 69 (1947) 542–553.
[15] S.J. Pennycook, Ultramicroscopy 30 (1989) 58–69.
[16] B. Fultz, J.M. Howe, Transmission Electron Microscopy and Diffractometry of Materials, Springer, Berlin, 2001.
[17] E. Kern, Mineralogisch-Petrograph. Inst., University of Heildelberg, Germany, ICDD, 1993.
[18] H.E. Swanson, E. Tatge, National Bureau of standards circular no. 539, in: US Government Printing Office, Washington, DC, vol. I, 1953.
[19] I. Moysan, V. Paul-Boncour, S. Thiébaut, E. Sciora, J.M. Fournier, R. Cortes, S. Bourgeois, A. Percheron-Guégan, J. Alloys Compd. 322 (2001) 14–20.
[20] (a) E. Xue, K. Seshan, J.R.H. Ross, Appl. Catal. B 11 (1996) 65–79;
(b) R.E. Lakis, C.E. Lyman, H.G. Stenger Jr., J. Catal. 154 (1995) 261–275.
[21] A.J. Renouprez, A. Malhomme, J. Massardier, M. Cattenot, G. Bergeret, Sulphur resistant palladium–platinum catalysts prepared from mixed acetylacetonates studies in surface science and catalysis, in: F.V.M. Avelino Corma, Segrario Mendioroz and José Luis G. Fierro (Eds.), 12th International Congress on Catalysis, Proceedings of the 12th ICC, Elsevier, 2000, pp. 2579–2584.
[22] O. Ezekoye, Ph.D. Thesis, 2010.
[23] A. Morlang, U. Neuhausen, K.V. Klementiev, F.-W. Schütze, G. Miehe, H. Fuess, E.S. Lox, Appl. Catal. B 60 (2005) 191–199.
[24] N. Toshima, M. Harada, T. Yonezawa, K. Kushihashi, K. Asakura, J. Phys. Chem. 95 (1991) 7448–7453.
[25] A. De Sarkar, M. Menon, B.C. Khanra, Appl. Surf. Sci. 182 (2001) 394–397.
[26] (a) D. Cheng, S. Huang, W. Wang, Chem. Phys. 330 (2006) 423–430;
(b) A.A. Herzing, M. Watanabe, J.K. Edwards, M. Conte, Z.-R. Tang, G.H. Hutchings, C.J. Kiely, Faraday Discuss. 138 (2008) 337–351;
(c) V. Mazumder, M. Chi, K.L. More, S. Sun, J. Am. Chem. Soc. 132 (2010) 7848–7849.
[27] J. Andersson, M. Antonsson, L. Eurenius, E. Olsson, M. Skoglundh, Appl. Catal. B 72 (2007) 71–81.
[28] P.J.F. Harris, E.D. Boyes, J.A. Cairns, J. Catal. 82 (1983) 127–146.
[29] A.K. Datye, Q. Xu, K.C. Kharas, J.M. McCarty, Catal. Today 111 (2006) 59–67.

[30] (a) C.G. Granqvist, R.A. Buhrman, J. Catal. 42 (1976) 477–479;
(b) D. Bhatia, R.W. McCabe, M.P. Harold, V. Balakotaiah, J. Catal. 266 (2009) 106–119.
[31] B.M. Weiss, E. Iglesia, J. Catal. 272 (2010) 74–81.
[32] J. Jelic, K. Reuter, R. Meyer, Chem. Catal. Chem. 9999 (2010). NA.
[33] E. Lundgren, J. Gustafson, A. Mikkelsen, J.N. Andersen, A. Stierle, H. Dosch, M. Todorova, J. Rogal, K. Reuter, M. Scheffler, Phys. Rev. Lett. 92 (2004) 046101.